NANO LETTERS
Letter
Cite This: Nano Lett. 2019, 19, 8811−8820
pubs.acs.org/NanoLett

Sparked Reduced Graphene Oxide for Low-Temperature Sodium-Beta Alumina Batteries

Dana Jin,[†,‡,○] Hae Gon Lee,[§,○] Sangjin Choi,[†,‡] Sungsoon Kim,[†,‡] Younki Lee,[∥] Sori Son,[⊥] Yoon-Cheol Park,[⊥] Joon Sang Lee,[*,§] Keeyoung Jung,[*,⊥] and Wooyoung Shim[*,†,‡,#,▽]

[†]Department of Materials Science and Engineering, Yonsei University, Seoul 03722, Korea
[‡]Center for Multi-Dimensional Materials, Yonsei University, Seoul 03722, Korea
[§]Department of Mechanical Engineering, Yonsei University, Seoul 03722, Korea
[∥]Department of Materials Engineering and Convergence Technology, Gyeongsang National University, Jinju 52828, Korea
[⊥]Materials Research Division, Research Institute of Industrial Science & Technology, Pohang 37673, Korea
[#]Yonsei-IBS Institute, Yonsei University, Seoul 03722, Korea
[▽]Center for NanoMedicine, Institute for Basic Science (IBS), Seoul 03722, Korea

Supporting Information

ABSTRACT: Wetting Na metal on the solid electrolyte of a liquid Na battery determines the operating temperature and performance of the battery. At low temperatures below 200 °C, liquid Na wets poorly on a solid electrolyte near its melting temperature (T_m = 98 °C), limiting its suitability for use in low-temperature batteries used for large-scale energy-storage systems. Herein, we propose the use of sparked reduced graphene oxide (rGO) that can improve the Na wetting in sodium-beta alumina batteries (NBBs), allowing operation at lower temperatures. Experimental and computational studies indicated rGO layers with nanogaps exhibited complete liquid Na wetting regardless of the surface energy between the liquid Na and the graphene oxide, which originated from the capillary force in the gap. Employing sparked rGO significantly enhanced the cell performance at 175 °C; the cell retained almost 100% Coulombic efficiency after the initial cycle, which is a substantial improvement over cells without sparked rGO. These results suggest that coating sparked rGO is a promising but simple strategy for the development of low-temperature NBBs.

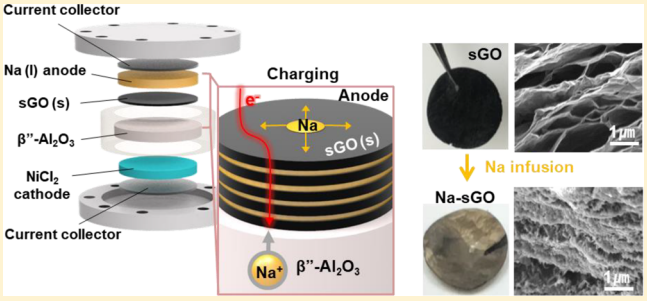

KEYWORDS: *sodium-beta alumina battery, sparked reduced graphene oxide, liquid metal wetting*

High-temperature Na-based batteries, e.g., Na/S and sodium/metal halide (Na/$MeCl_2$) batteries, are based on Na ion transport through the β''-Al_2O_3 solid electrolyte as a Na^+-conducting membrane.[1−4] During discharge at elevated temperatures, liquid Na is oxidized at the Na (anode)/β''-Al_2O_3 (electrolyte) interface, and the resulting Na^+ moves through the β''-Al_2O_3 solid electrolyte to react with S (Na/S battery) or Cl (Na/$MeCl_2$ battery) that is reduced at the cathode, forming Na_2S_5 and NaCl, respectively.[5,6] Such sodium-beta alumina batteries (NBBs) have been employed for large-scale energy-storage applications, but elevated temperatures are required for electrochemical activity, delaying the realization of low-temperature NBBs that bypass expensive manufacturing but ensure safety.[7−9]

Several features are critical to low-temperature NBBs. First, at a low T (but still above $T_{m,Na}$ = 98 °C, i.e., the melting temperature of Na), the sufficient ionic conductivity for β''-Al_2O_3 should be retained at the level of high-temperature ionic conductivity (ranging from 0.2 to 0.4 $S{\cdot}cm^{-1}$).[10] This requires chemistry control, such as doping of divalent cations (e.g., Mg^{2+}, Ni^{2+}, Zn^{2+}, and Cu^{2+} ions) into β''-Al_2O_3[11,12] as well as microstructure control, including vacancy generation and large-grain growth.[13] Second, because the liquid Na wetting area on the β''-Al_2O_3 surface determines the active area of the Na^+ pathway (Figure S1), liquid Na wetting at a low T should be preserved. The liquid Na wetting generally decreases as the temperature T decreases because of an increase in the surface energy $d\gamma = -S_s dT$, where S_s represents the surface entropy ($S_s > 0$).[14−16] Thus, we recently introduced a Bi metal coating on β''-Al_2O_3 and showed that through the formation of metallic islands, the liquid Na wetting increased even at low temperatures (175 °C), and hence, the cell performance of the Na/$NiCl_2$ battery was improved.[17]

Received: September 4, 2019
Revised: November 15, 2019
Published: November 26, 2019

DOI: 10.1021/acs.nanolett.9b03646
Nano Lett. 2019, 19, 8811−8820

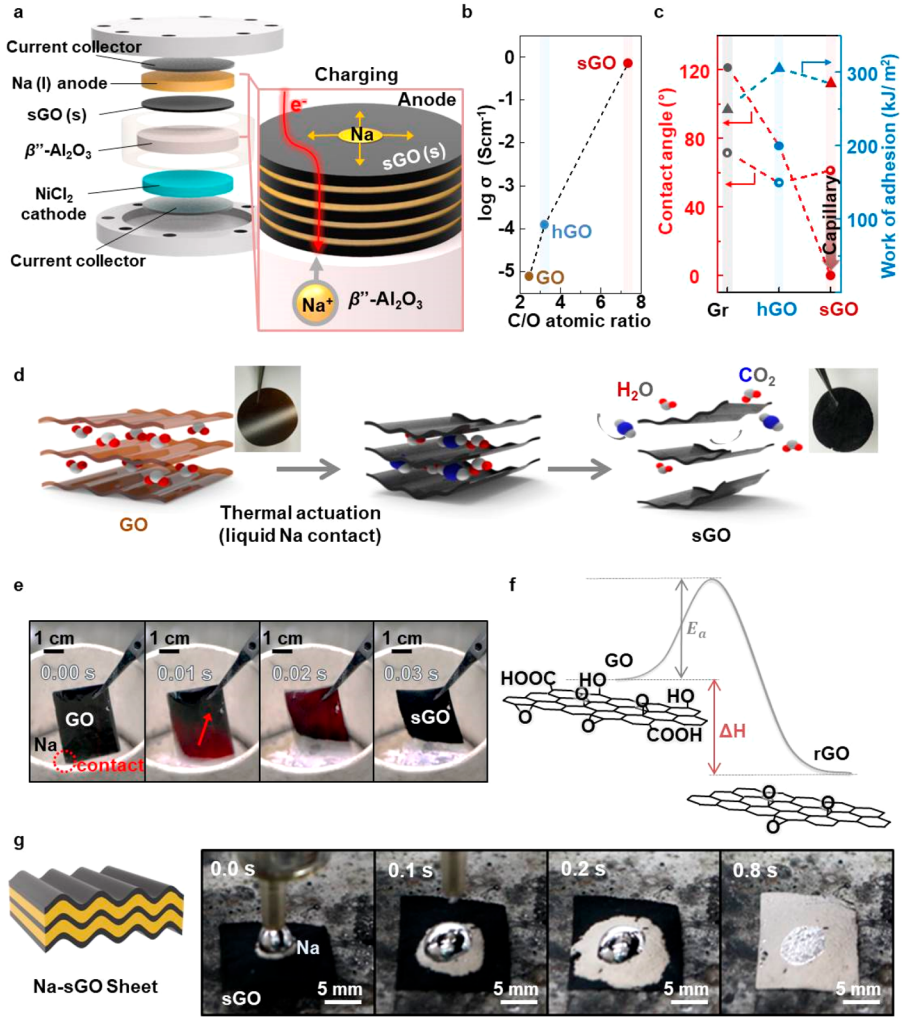

Figure 1. Synthesis and sodiophilic characteristic of the sparked rGO film. (a) Schematic of the Na-$NiCl_2$ cell using the sparked rGO film. (b) C/O atomic ratio dependence of the electrical conductivity. (c) Comparison between the measured liquid Na contact angles (close circle) and the calculated contact angles (open circle) of Gr (gray), heated rGO (blue), and sparked rGO (red). The calculated contact angles were determined using the work of adhesion values (triangle) obtained via MD simulations. (d) Schematic of the synthesis process for the sparked rGO film. Inset: photographs of the GO and sparked rGO films. (e) Time-lapse photographs of the spark reaction of the GO film triggered by contact with liquid Na (300 °C). (f) Schematic of the activation energy of the thermal reduction. (g) Time-lapse photograph of liquid Na infusion into the sparked rGO film.

This metal coating approach can be explained according to the thermodynamic work of adhesion w_{adh}, which is correlated with the surface energy of liquid Na $\gamma_{l,v}$, the surface energy of the solid surface $\gamma_{s,v}$, and the interfacial energy $\gamma_{l,s}$, as described by the Young–Dupre equation $w_{adh}/\gamma_{l,v} = 1 + \cos\theta$, where θ represents the contact angle and $\gamma_{l,v}$ is replaced by $(\gamma_{s,v} - \gamma_{l,s})/\cos\theta$ from Young's equation.[18] With a given $\gamma_{\text{liquid Na},v}$ of 192.41 mJ/m^2 at 450 K,[19] for example, an appropriate metal coating on the β''-Al_2O_3 surface, such as Ni, Sn, Bi, or Pb, can increase w_{adh} with liquid Na and then reduce θ, consequently improving the wetting.[20−23] In such cases, enhanced liquid Na–metal wetting originates from the increased w_{adh}. Given that γ is a function of T, P, and the crystal plane and is an intrinsic property of the material,[14] the choice of metals inevitably determines the liquid Na wettability; therefore, there is little room to improve the Na^+ transport. On the nanoscale, coated metal islands (or nanoparticles with small radius r) have a higher chemical potential μ_M and thus a higher vapor pressure of a particle, P_r, rather than a change in γ.[14,24] In general, this high vapor pressure leads to a low melting temperature T_m and increased solubility, which differ from those for the bulk material and make the metal coating readily react with liquid Na. While taking advantage of metal passivation, this approach, where the metal ions are considered as potential impurities, hinders Na ion transport and prevents the full utilization of the contact area owing to the presence of metal impurities on the surface of the β''-Al_2O_3. An ideal coating material provides complete liquid Na wetting beyond the surface energy γ (or chemical potential μ) of the material but does not have solubility in liquid Na.

Herein, we report a new approach for achieving high-performance low-temperature NBBs via the incorporation of sodiophilic sparked reduced graphene oxide (rGO) layers that exhibit complete liquid Na wetting. This approach utilizes capillary force for complete wetting that would otherwise be fundamentally limited by the surface energy γ and vapor pressure P_r of the coated materials.[25] Compared with previous metal (Li or Na)-ion batteries, where sparked rGO layers have been used for such metal reservoirs as an anode,[26−30] sodiophilic sparked rGO layers in NBBs provide potential

DOI: 10.1021/acs.nanolett.9b03646
Nano Lett. 2019, 19, 8811−8820

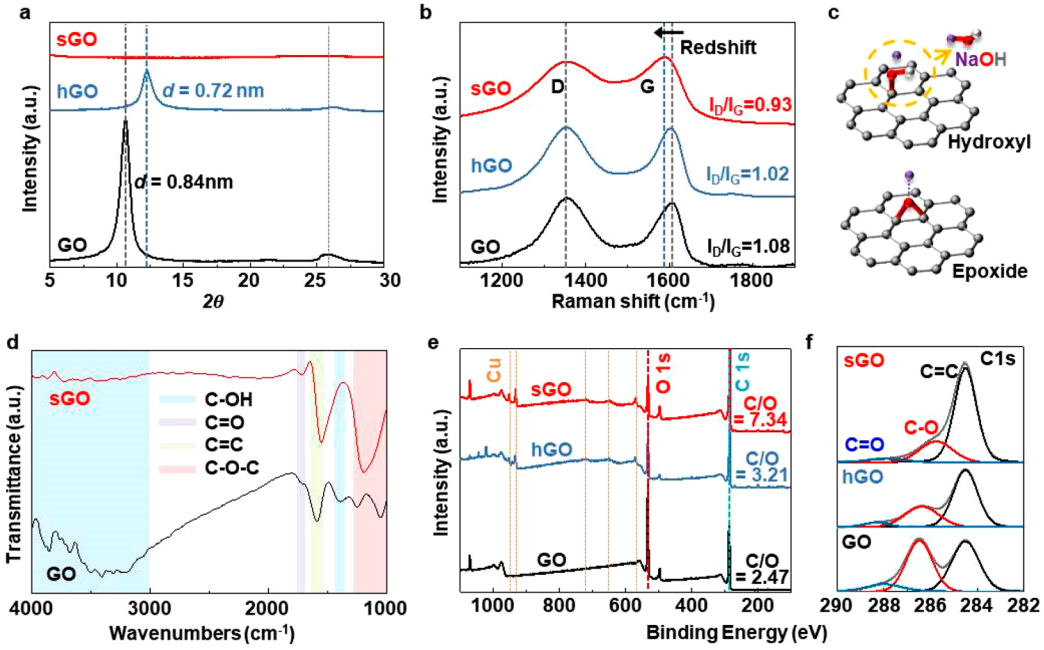

Figure 2. Characterization of the GO films. (a) XRD patterns and (b) Raman spectra of GO (black line), heated rGO (blue line), and sparked rGO (red line). (c) Schematic of the reactions of oxygen functional groups with Na atoms: hydroxyl (top) and epoxy (bottom). (d) FT-IR spectra of GO (black line) and sparked rGO (red line). (e) XPS spectra and (f) deconvoluted XPS C 1s spectra of GO, heated rGO, and sparked rGO.

advantages, e.g., low-temperature wettability, low overpotential, cyclability, and cell efficiency. First, the capillary force induced between the layers with nanogaps leads to complete liquid Na wetting if $(\gamma_{s,v} - \gamma_{l,s})/\gamma_{l,v}$ has a positive value ($\cos\theta > 0$),[18] indicating (i) that the Na nucleation and growth are sufficiently rapid to form liquid Na when the battery is charged and (ii) that the area of the Na^+ passway at the Na (anode)/β''-Al_2O_3 (electrolyte) interface is maximized when the battery is discharged. Second, through the spark reaction, the electrical conductivity of the sparked rGO can be restored, which not only improves the distribution of active sites for Na reduction but also can provide an inert anode scaffold that does not engage in alloy formation. Third, owing to the insolubility of the sparked rGO in Na at the operating temperatures (<200 °C), there is no issue regarding Na^+ transport in the context of metal impurities on the surface of the β''-Al_2O_3. Fourth, as a result, employing the sparked rGO layers significantly improves the cell performance by >2749% with regard to the cell capacity and by 149% with regard to the overpotential compared with bare cells (at the fifth cycle). Below, we describe the fabrication, structural analysis, and wetting behavior of the sparked rGO layers based on a molecular dynamics simulation as well as the integration of the layered element into a Na/$NiCl_2$ battery cell for low-temperature NBBs.

Our single Na-$NiCl_2$ cell consists of a liquid Na (anode)/β''-Al_2O_3 (solid electrolyte)/$NiCl_2$ (cathode) with a liquid secondary electrolyte ($NaAlCl_4$), and we insert a layered sparked rGO film sandwiched between the anode and the solid electrolyte (Figure 1a). Typically, when a Na-$NiCl_2$ cell is assembled, its anode is initially almost empty with a small amount of Na in contact with the β''-Al_2O_3. Upon the charging of the cell during the first cycle, Na^+ ions formed at the cathode diffuse to the anode through β''-Al_2O_3 and then fill the empty anode space via one-electron reduction of the Na^+ ion. The higher wettability of liquid Na on the surface of β''-Al_2O_3 induces better charging characteristics such as a low overpotential.[22,23,25] In this regard, we utilize sparked rGO during charging. First, when Na^+ ions diffuse on the β''-Al_2O_3 surface, they are reduced to liquid Na by accepting electrons from sparked rGO at the sparked rGO/β''-Al_2O_3 interface (stage I, Figure S2a); thus, heterogeneous nucleation of liquid Na occurs on the conductive sparked rGO. For heterogeneous nucleation of Na on the sparked rGO surface, the energy barrier (ΔG_r^*) for forming a nucleus having the shape of a spherical cap with a critical radius of curvature r^* is $\Delta G_r^* = \left(\frac{16\pi\gamma^3}{3\Delta G_V^{\ 2}}\right) f(\theta)$, where ΔG_V is the volumetric Gibbs free energy change per unit volume and γ is surface energy per unit length along the Na nucleus.[14] The $f(\theta)$ is the ratio of the volume of the heterogeneous nucleus (the cap) to the volume of the sphere with the same radius of curvature. Sparked rGO with a sodiophilic nature has a low contact angle (θ) with liquid Na, which induces low $f(\theta)$ (Figure S2b); further, it has a low energy barrier for nucleation (Figure S2c). The sparked rGO film also provides an electrical path over the entire surface of the β''-Al $_2O_3$ for Na^+ reduction. The conductivity of the sparked rGO film is significantly higher than that of the samples before the spark reaction, i.e., the GO and heated rGO (130 °C for 1 h); it is almost 5 and 4 orders of magnitude higher, respectively (Figure 1b). Second, the significant growth of liquid Na is expected (stage II, Figure S2a) owing to the wettability of the sparked rGO induced by the capillary force (Figures 1c and S3). The liquid Na contact angle on the sparked rGO is 0° (closed red circle, Figure 1c) owing to the induced capillary force between the sparked rGO layers and the infiltration of liquid Na into the porous sparked rGO (Figure S4), which is far smaller than the intrinsic contact angle of the sparked rGO (θ = 61.3°, open red circle, Figure 1c) calculated using the w_{adh} (red triangle, Figure 1c). Thus, further flow leads to the conformal filling of liquid Na, which

DOI: 10.1021/acs.nanolett.9b03646
Nano Lett. 2019, 19, 8811−8820

represents good wetting of liquid Na at the sparked rGO/β''-Al$_2$O$_3$ interface (stage III, Figure S2a).

Following this concept, we fabricated sparked rGO by using GO films (Figure S5) as a starting material (Figure 1d). In this study, the production of the sparked rGO benefited greatly from thermal reduction rather than a chemical reduction process because thermal reduction involves no external impurities.[31] In this thermal reduction, the layered GO film was partially placed in contact with molten Na. A spark reaction occurred immediately and propagated across the entire film (from 0.02 to 0.04 s, Figure 1e), driven by the exothermic reaction (Figure 1f), expanding the film into a porous structure (Figure 1d and Movie S1). In a spark reaction, the structure of the layered sparked rGO film, including oxygen functional groups and the interlayer gap, can be tuned by the fast kinetic process of thermal reduction (Figure S6). For example, the explosive rapid thermal expansion is initiated when the rate of decomposition of GO exceeds the rate of diffusion of gas products (e.g., CO, CO_2, and H_2O); thus, a threshold overpressure that overcomes the van der Waals forces between the GO layers can arise.[30,32−36] In contrast, a heating process, which is a slow process to generate heated rGO, transforms the GO film into an rGO film with an even smaller interlayer gap owing to the removal of oxygen functional groups on the rGO surface (Figure S7).[37,38] When the Na drop was transferred to the surface of the sparked rGO film, liquid Na was infused into the sparked rGO sheets instantly (<1 s) and spread across the entire sparked rGO film owing to the effects of the sodiophilic nature of the sparked rGO and the capillary force produced by the nanogaps (Figure 1g and Movie S2). This infusion was also observed for liquid Li and K (Figure S8). In contrast to the sparked rGO film, the heated rGO film exhibited significantly slower infusion of liquid Na, mostly because of the small interlayer gap (Figure S9).

Next, we investigated the microstructure changes of the GO film upon the spark reaction. First, the change in the interlayer gap of the GO films due to the spark reaction was examined via X-ray diffraction (XRD) analysis (Figure 2a). A pristine GO film (black line, Figure 2a) exhibited a typical (002) peak at 2θ = 10.52°, corresponding to an interlayer gap of approximately 0.84 nm, which was larger than the graphite interlayer gap (0.34 nm) and resulted from the oxygen functional groups.[37] A smaller and broader graphitic peak at 2θ = 26.18° was also observed, corresponding to an interlayer gap of approximately 0.34 nm. These results indicate that the heterogeneous nature of GO comprised more sp^3 bonds from the oxidized region and less sp^2 bonds from the graphitic region. The heated rGO film (blue line, Figure 2a) exhibited a diffraction peak at 2θ = 12.3°, which was slightly shifted toward the higher-angle side compared with the GO peak, indicating that the interlayer gap was reduced to approximately 0.72 nm. The slight reduction of the interlayer gap could have been induced by the removal of preabsorbed moisture between GO sheets.[39] After the spark reaction of the GO film, the sharp peak at 2θ = 10.52° disappeared, indicating (i) that the distance between layers was increased above approximately 3 nm and (ii) that oxygen functional groups were efficiently removed during the spark reaction (red line, Figure 2a). Additionally, the physical adsorption−desorption analysis of N_2 was performed to investigate the change in pore structure for each sample (Figure S10). The hysteresis in the adsorption−desorption isotherms of all samples was of the H3 type according to the International Union of Pure and Applied Chemistry (IUPAC) classification and indicated a plane-parallel structure.[40−42] The sparked rGO had a larger Brunauer−Emmett−Teller (BET) specific surface area (292.83 m^2/g, Figure S10a) compared with that of the GO (5−50 m^2/g, Figure S10b and Table S1) and the heated rGO (5.70 m^2/g, Figure S10c).[40,41,43,44] The pore-size distribution (PSD) analysis revealed that majority of this vast surface area of the sparked rGO originated from interlayer gaps with a size of approximately 4 nm (Figure S10d); further, a wide range of pore size (pores from 3 nm up to 80 nm) of sparked rGO film indicates irregular stacking of rGO sheets relatively.[45] The interlayer space of sparked rGO sheets provides a horizontal path for liquid Na, and irregularity of stacking provides higher transverse path for liquid Na (Table S2). However, the GO (Figure S10e) and heated rGO (Figure S10f) films did not show the PSD periodicity, which was observed in sparked rGO; this was due to the relatively ordered and close-packed structure. Second, this thermal reduction was confirmed by Raman spectra. As shown in Figure 2b, the intensity ratio between the D band and the G band (I_D/I_G) was reduced after heating or the spark reaction owing to the removal of functional groups and the recovery of the sp^2 hybridization. The G band of pristine GO (black line, Figure 2b) was located at 1609 cm^{-1}, whereas the G bands of heated rGO (blue line, Figure 2b) and sparked rGO (red line, Figure 2b) were red-shifted to 1603 and 1589 cm^{-1}, respectively, providing further evidence of the recovery of the sp^2 structures via the removal of oxygen functional groups.[46] Up to this point, the sparked rGO film possessed more graphitic domains and less oxidized domains than the pristine GO and heated rGO films.

Additionally, we characterized the reductions in hydroxyl (−OH) and epoxy (C−O−C) groups due to the spark reaction. Given that the absorption of Na atoms on these oxygen functional groups through the transfer of their valence electrons to oxygen was favorable, the sodiophilic nature of the sparked rGO film is partially attributed to these oxygen functional groups. However, hydroxyl group (−OH) can chemically react with Na because of the high binding energy with Na atoms (−2.84 eV), resulting in the generation of NaOH as an unnecessary byproduct (top, Figure 2c).[47] In contrast, epoxy (C−O−C) has a lower binding energy with Na atoms (−1.97 to −2.09 eV) and generally does not form sodium oxide byproducts (bottom, Figure 2c).[47] In the words of an electrochemist, epoxy groups are redox-active; therefore, the presence of epoxy on GO is more desirable with regard to both wetting and the absence of impurities. As shown in Figure 2d, the hydroxyl group was almost removed by the spark reaction, according to Fourier transform infrared (FT-IR) spectroscopy. Before the spark reaction, a strong peak corresponding to −OH stretching (broad peak beyond 3000 and 1390 cm^{-1}) was detected, which revealed the presence of a large proportion of −OH (black line, Figure 2d).[46] Simultaneously, characteristic peaks of other surface groups, such as carbonyl (C═O) (1716 cm^{-1}) and epoxy (C−O−C) (1249 and 1052 cm^{-1}), were observed.[46] In contrast, after the spark reaction, the −OH peak became almost undetectable, confirming the removal of both residual water and surface −OH groups (blue shaded area, Figure 2d). However, the peaks of the other more stable O-containing surface moieties (e.g., C−O−C) were retained in both the pristine GO and sparked rGO. Additionally, in X-ray photoelectron spectroscopy (XPS), a significantly increased C/O atomic ratio was

DOI: 10.1021/acs.nanolett.9b03646
Nano Lett. 2019, 19, 8811−8820

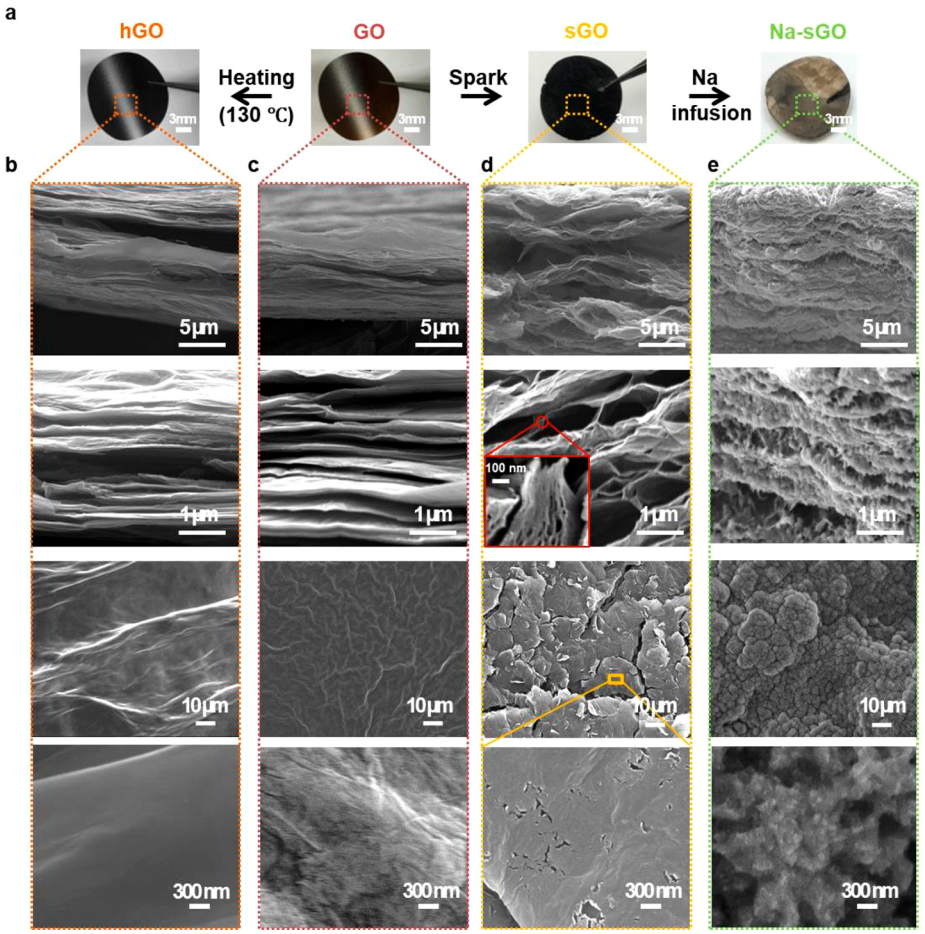

Figure 3. Morphological analysis of GO films. (a) Photographs of heated rGO, GO, sparked rGO, and liquid Na-infused sparked rGO. Cross-sectional SEM images (first and second rows) and in-plane SEM images (third and fourth rows) of (b) heated rGO, (c) GO, (d) sparked rGO, and (e) liquid Na-infused sparked rGO. The inset of panel d represents a high-magnification SEM image, which reveals the nanogaps between sparked rGO layers.

observed for sparked rGO (7.34) compared with GO (2.47), indicating a significant reduction in O after the spark reaction (Figure 2e). In the deconvoluted C 1s spectra, the intensity corresponding to the C−OH peak (286.5 eV) was reduced by 52% of the original value (for GO) after the spark reaction (Figure 2f).

We subsequently investigated the liquid Na wetting in the sparked rGO. Figure 3a shows digital camera images, and Figures 3b−e show corresponding cross-sectional (first and second rows) and in-plane (third and fourth rows) field-emission scanning electron microscopy (SEM) images of the heated rGO, pristine GO, sparked rGO, and Na-infused sparked rGO films, respectively. The pristine GO film exhibited the typical densely stacked structure (Figure 3c). It was difficult to observe the differences between the structures of the heated rGO film (Figure 3b) and the pristine GO film because the difference in the gap size between the heated rGO (0.72 nm) and GO (0.84 nm) films was small. After the spark reaction, significantly enlarged interlayer spacing was clearly observed with uniform nanogaps between the sparked rGO layers, which provided a scaffold structure for storing the liquid Na (inset of second row, Figure 3d). This increased the surface area of the sparked rGO (Figure S10a). An in-plane SEM image indicated that the pristine GO had a wrinkled surface (third and fourth rows, Figure 3c), and the heated rGO had a smooth surface with fewer wrinkles (third and fourth rows, Figure 3b). After the spark reaction, cracks and pores were formed in the sparked rGO film (third and fourth rows, Figure 3d). The nanopores in the surface of sparked rGO sheets were also observed by using high-resolution transmission electron microscopy (HR-TEM) images (Figure S11). Once Na was infused into the sparked rGO film through the cracks and pores of the surface, as shown in Figure 3e, the nanogaps were uniformly filled by liquid Na, as discussed previously, and the surface of the sparked rGO film was covered with Na (for details regarding the contact-angle measurements, see Figure S12).

In light of the structural analysis and the observation of Na infusion, we investigated the liquid Na wetting on graphene (Gr), heated rGO, and sparked rGO using molecular dynamics (MD) simulations. The simulation setup is shown in Figure 4a and Table S3, where one of the Gr, heated rGO, and sparked rGO channels bridged the feed reservoir (left) and permeate reservoir (right). A fixed number (46 216) of Na atoms (corresponding to a liquid Na density of 0.927 g/cm^3) was initially loaded in the feed reservoir, while the channel and the permeate reservoir were empty. The movement of Na atoms was triggered by the capillary-driven flow from the feed reservoir to the permeate reservoir through Gr, heated rGO, and sparked rGO channels. MD simulations were performed for 10 different interlayer gaps (d) of the channel (d = 0.34−3.92 nm), which were in the range of the interlayer gap of

DOI: 10.1021/acs.nanolett.9b03646
Nano Lett. 2019, 19, 8811−8820

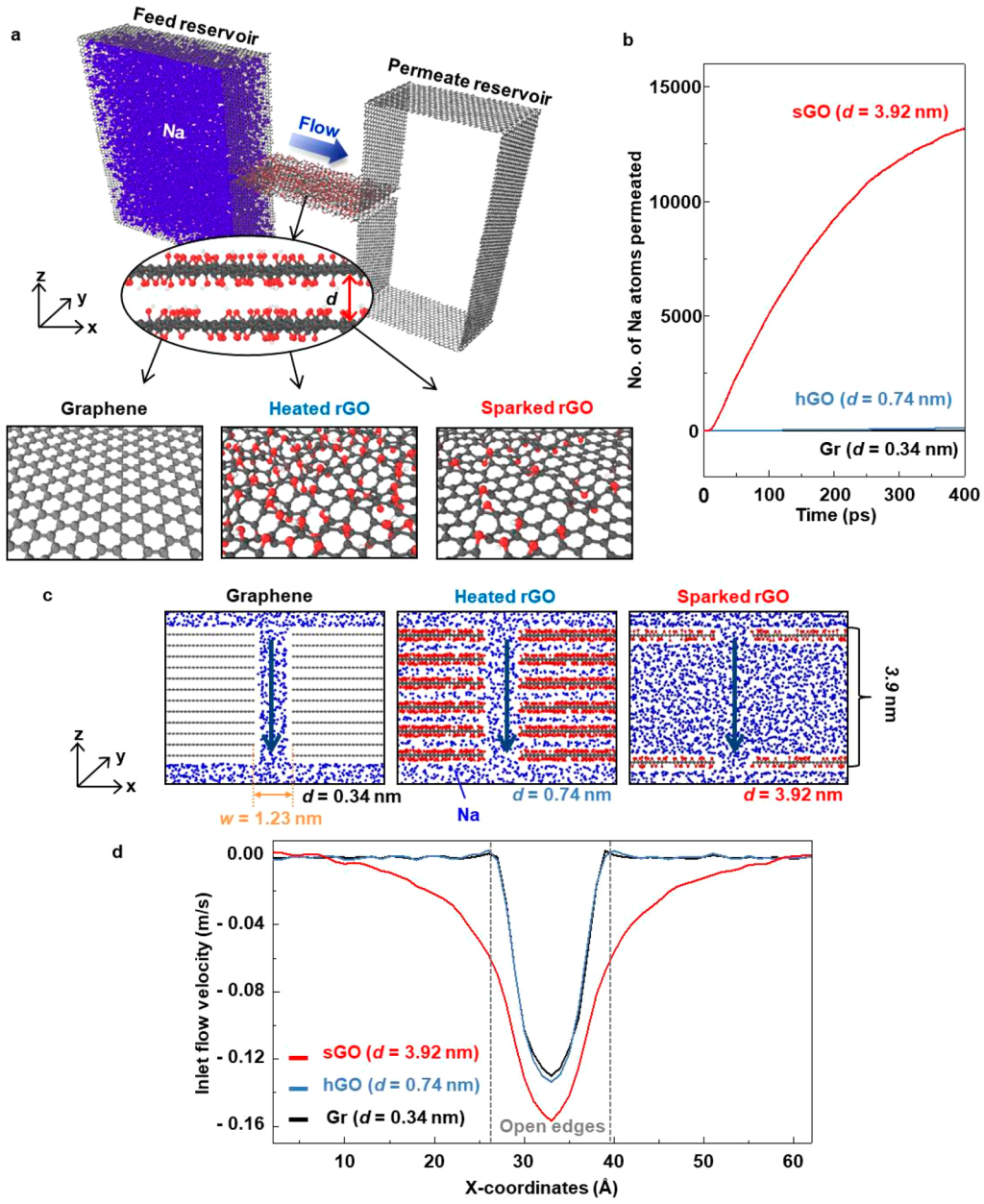

Figure 4. MD simulation of liquid Na transport in Gr (d = 0.34 nm), heated rGO (d = 0.74 nm), and sparked rGO (d = 3.92 nm) channels. (a) Side-view illustrations of the simulated cell: C atoms (gray), O atoms (red), H atoms (white), and Na atoms (blue). The detailed structures of the heated rGO and sparked rGO are presented at the bottom. (b) Numbers of Na atoms entering the permeate (right) reservoir through the Gr (black line), heated rGO (blue line), and sparked rGO (red line) channels. (c) Front-view illustrations of the simulated cell for the vertical flow of liquid Na. (d) Inlet flow−velocity profiles along the x-axis in the Gr, heated rGO, and sparked rGO sheets.

graphite (d = 0.34 nm), heated rGO (d = 0.34−1.35 nm, depending on the number of O functional groups), and the sparked rGO (d = ∼4 nm, Figure S10d). We (i) assumed that the oxygen functional groups of the heated rGO and sparked rGO were hydroxyl groups (−OH) and epoxy groups (C−O−C) on the C plane but that there were fewe oxygen functional groups for the sparked rGO; (ii) ignored the carboxyl (−COOH) and carbonyl (C═O) groups predominantly present at the edge of GO to focus on GO surface−liquid Na surface interactions;[48] and (iii) assumed that the oxygen functional groups were randomly distributed to both sides of the graphene C plane (bottom, Figure 4a). Detailed configuration information (e.g., O concentration, functional-group ratio) for both materials is presented in Table S4. The number of Na atoms entering the permeate reservoir through the Gr (d = 0.34 nm), heated rGO (d = 0.74 nm), and sparked rGO (d = 3.92 nm) channels was monitored as a function of time without the external pressure (Figure 4b). In the cases of the Gr (black line, Figure 4b) and heated rGO (blue line, Figure 4b), the noticeable permeation of Na atoms was not observed. However, for the sparked rGO, the flow rate was increased, indicating that the capillary force was dominant at this scale. The amount of Na atoms that permeated through the sparked rGO capillary (red line, Figure 4b) (13 193 atoms) was significantly larger than that for the Gr (0 atoms) and heated rGO capillaries (109 atoms) at 400 ps.

As well as a horizontal flow of liquid Na through the interlayer gap, we also established the liquid sodium vertical

DOI: 10.1021/acs.nanolett.9b03646
Nano Lett. 2019, 19, 8811−8820

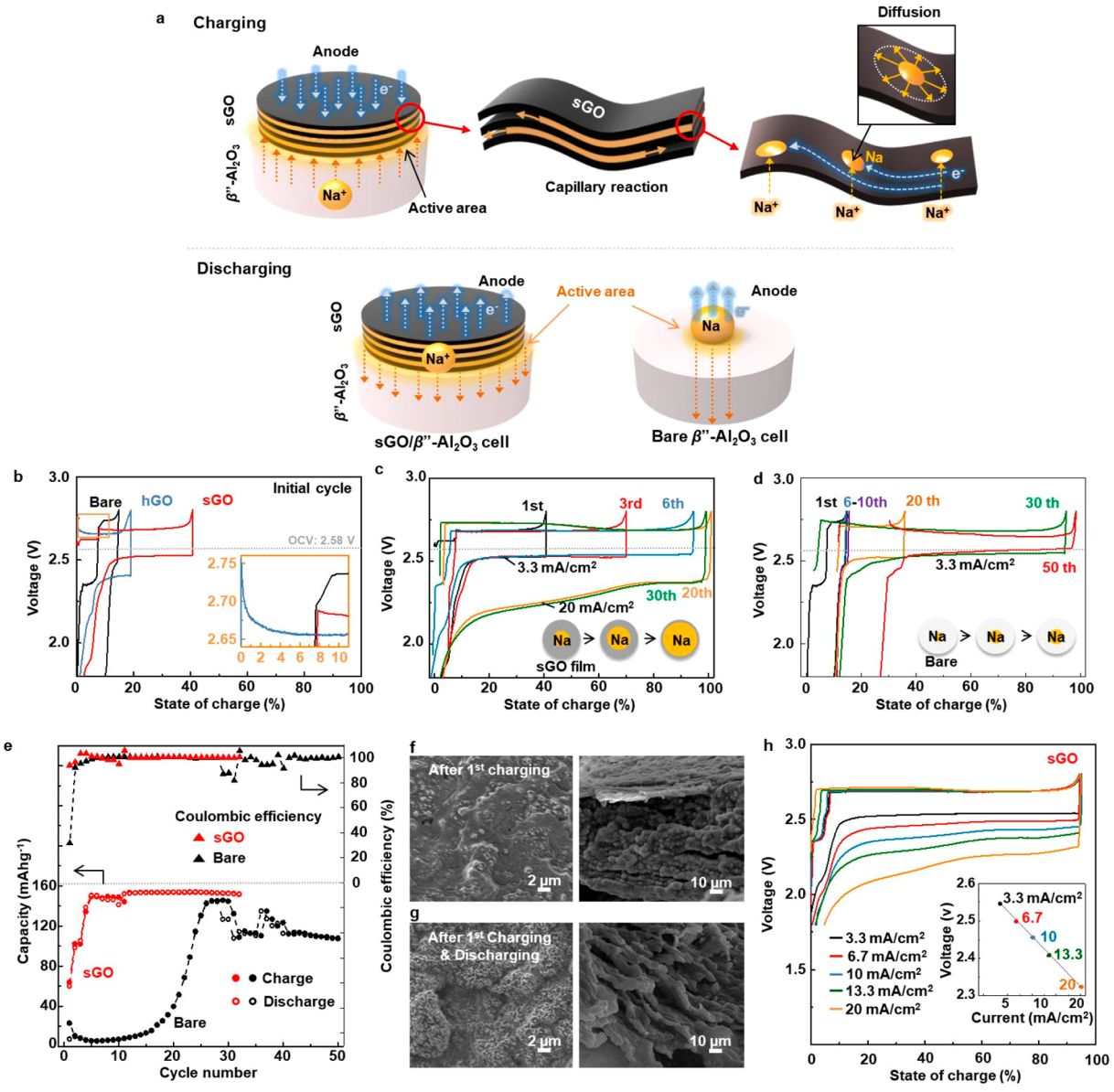

Figure 5. Electrochemical performance. (a) Schematic of the liquid Na filling process through the sparked rGO film in the anode during charging (top) and the active area of the sparked rGO-treated β''-Al_2O_3 (left) as well as the bare β''-Al_2O_3 (right) during discharge (bottom). (b) Initial charge and discharge profiles of the bare β''-Al_2O_3 (black line), heated rGO (blue line), and sparked rGO (red line) cells. The inset of panel b represents initial charge profiles during the beginning of the liquid Na reduction process. (c) Charge and discharge profiles of the sparked rGO cell for 30 cycles. (d) Charge and discharge profiles of the bare β''-Al_2O_3 cell for 50 cycles. (e) Charge (close circle) and discharge (open circle) profiles (bottom) of the sparked rGO cell (red) and bare cell (black) with the corresponding Coulombic efficiency (top). (f) In-plane (left) and cross-section (right) SEM images of sparked rGO films after first charge, and those after the first charge/discharge cycle can be observed in panel g. (h) Voltage profiles of sparked rGO cell with different discharging currents (3−20 mA/cm^2).

flow through the porous structure of the Gr, heated rGO, and sparked rGO sheet. The simulation setup for vertical flow is shown in Figure 4c. At a similar total sheet thickness of 3.9 nm, the Gr (d = 0.34 nm), heated rGO (d = 0.74 nm), and sparked rGO (d = 3.92 nm) sheets consisted of 12, 6, and 2 layers, respectively. For vertical transportation, the open edges were formed between sheets in each case; these had a width (w) of 1.23 nm, corresponding to the size of 4 linear graphene hexagons (Figure 4c). To maintain a steady state mass flux across the sheets, a force (10 MPa) along the z-axis is applied to all molecules located in the upper sodium slab. In the sparked rGO sheets, the liquid Na flowed into the open edges faster than that of the Gr and heated rGO sheets, as shown in Figure 4d. The average vertical flow velocity in sparked rGO sheet was also faster (0.116 m/s), compared to Gr (0.0751 m/s) and heated rGO (0.0761 m/s) sheets. These results originated from the lower resistance of the vertical flow of liquid Na through the open edges of the sparked rGO sheets due to a large interlayer gap (d = 3.92 nm). To investigate the degree of resistance that a sodium atom undergoes during flowing through the several open edges in each case, we calculate the potential mean force (PMF) values of a sodium atom along the z-coordinates (perpendicular to the open edges, Figure S13). The average PMF values in each Gr, heated rGO, and sparked rGO sheet were approximately 43.7, 39.8, and 27.2 kcal/mol, respectively. This result implies that

DOI: 10.1021/acs.nanolett.9b03646
Nano Lett. 2019, 19, 8811−8820

the sodium atoms are subjected to less resistance when a vertical transport occurs in the sparked rGO sheet rather than in the other sheets. The lower resistance of sparked rGO is most possibly caused by the fact that, from an atomic perspective, the atomic density interacting with sodium atoms is the smallest in the sparked rGO system; this is due to the large interlayer gap.

Finally, we demonstrated the applicability of the sparked rGO film as a "wetting sheet" at the liquid Na anode/solid electrolyte (β''-Al_2O_3) interface in NBBs. During charging, Na^+ is transported across the β''-Al_2O_3 from the cathode to the liquid Na anode. The transport, distribution, and nucleation reaction are significantly affected by the wetting property (top, Figure 5a), as indicated by Figure 1a. The wetting property also impacts the discharging process, in that a low cell resistance is obtained when sufficient Na wetting (large active area) is realized (bottom, Figure 5a). We characterized the charge/discharge behavior of Na-$NiCl_2$ cells (Figure 5a) to investigate the effect of the sparked rGO film at 175 °C. Three different surface modifications of the anode sides of the β''-Al_2O_3 were prepared: (i) bare β''-Al_2O_3, (ii) heated rGO/β''-Al_2O_3, and (iii) sparked rGO/β''-Al_2O_3. These heated rGO and sparked rGO films were placed between the current collector and β''-Al_2O_3 during the cell assembly (left, Figure 1a). To investigate the initial wetting performance of the cells, the voltage profiles of the initial cycle were compared in Figure 5b. At the beginning of the liquid Na reduction process on the sparked rGO surface (third schematic at the top, Figure 5a), a slightly higher voltage (2.688 V) was recorded (inset, Figure 5b) when compared with the voltage plateau (2.680 V). This small increase in the voltage (0.008 V) was induced by the nucleation overpotential.[49−51] However, bare β''-Al_2O_3 and heated rGO exhibited far higher voltages of 2.736 and 2.746 V, respectively; this was observed at the beginning of the liquid Na reduction due to the poor Na wetting and significantly lower electrical conductivity compared with the sparked rGO. Additionally, the sparked rGO cell exhibited a higher capacity (40.7% state of charge (SOC); represented by the red curve in Figure 5b) than the heated rGO cell (19.1% SOC; represented by the blue curve in Figure 5b) and bare cell (14.7% SOC; represented by the black curve in Figure 5b). This indicates the presence of a larger active area of the sparked rGO cell. The large interlayer gaps of the sparked rGO allowed the full permeation of the liquid Na, as indicated by the MD techniques and the wetting test. Similarly, in the initial discharging process, the sparked rGO exhibited a far lower overpotential than the heated rGO and bare β''-Al_2O_3 cell; this was also induced by the sufficient Na wetting and the large active area of the sparked rGO (bottom, Figure 5a and Figure S14).

During a cycling test with a cutoff voltage between 1.8 and 2.8 V, the sparked rGO cell (Figure 5c, with a constant charge current of 10 mA (3.3 mA/cm^2) and different discharge current of 10−60 mA (20 mA/cm^2)) exhibited a low overpotential and stable cycles; this was in contrast to the bare β''-Al_2O_3 cell (Figure 5d, with a constant charge and discharge current of 10 mA). Additionally, the charging capacity of the sparked rGO cell increased during cycling from 40.7% SOC (64.0 mAh/g) at the first cycle to 97.5% SOC (153 mAh/g) at the 30th cycle (Figure 5c). The increase in the capacity was probably due to an increase in the active area caused by liquid Na infusion and spreading in the sparked rGO film during cycling (inset, Figure 5c). The Coulombic efficiency plot (red triangle, Figure 5e) indicated that almost 100% of the efficiency was retained after 32 cycles. The results suggest that the sparked rGO film provided a stable channel for liquid Na to flow during the charge/discharge process. The initial cycle exhibited a lower Coulombic efficiency (93%) because of the presence of residual liquid Na in the sparked rGO film after discharge. During cycles, slight fluctuation of Coulombic efficiency is induced from cycles 8−11 of the sparked rGO cell by increasing the discharge current. However, the bare β''-Al_2O_3 cell (Figure 5d) possessed small limited irregular capacities with higher overpotential; this was due to the poor Na wetting property, and consequently the small contact area between the Na and β''-Al_2O_3 (inset, Figure 5d). The high fluctuation in Coulombic efficiency (black triangle, Figure 5e) was also observed due to the irregular contact area of Na and β''-Al_2O_3 at each cycle (bottom, Figure 5a).

Additionally, to confirm the stability of the sparked rGO film during charge and discharge, the microstructures of the sparked rGO film were analyzed using SEM images after the cell test (Figures 5f and 5g). After the first charge, the surface of the sparked rGO sheet was homogeneous and smooth; this was due to the uniform coating of the liquid Na (left, Figure 5f) and also because of the fact that majority of the interlayer gaps were filled with liquid Na (right, Figure 5f and Figure S15a). After the first discharge, the surface pores and interlayer gaps originally occupied by liquid Na appeared again (right, Figure 5g and Figure S15b); these comprised of a small amount of residual liquid Na on the surface of sparked rGO sheets (left, Figure 5g). After the cycling test (17 cycles), the layered structure of the sparked rGO film was also preserved (for details regarding the structure analysis, see Figure S16).

To test the rate capability of the sparked rGO cell, the cell was cycled with different discharging currents of 10, 20, 30, 40, and 60 mA (20 mA/cm^2) and charging current of 10 mA. The capacity of the cell decreased slightly with an increase in the discharge current; however, the cell retained above 90% of the theoretical capacity (157 $mAhg^{-1}$) at each discharge current (Figure 5h). For example, the discharge capacity was 95.8% SOC (150.5 mAh/g) at a current of 10 mA. When the current was increased to 60 mA (20 mA/cm^2), the discharge capacity of the cell retained was 90% SOC (141.3 mAh/g). As the discharge current increased, the voltages at the beginning of discharge (BOD) decreased linearly (inset, Figure 5h). These results indicate that the stable contact area of liquid Na/β''-Al_2O_3 was preserved at each discharge current in the range of 10−60 mA (20 mA/cm^2).

These studies indicate that sparked rGO on the β''-Al_2O_3 surface can effectively enhance the wetting of liquid Na and the cell performance, thus providing a facile approach for realizing low-temperature NBBs. Compared with a bare β''-Al_2O_3 electrolyte, the sparked rGO coating, which is not limited by the surface energy or solubility, provides better cell reaction performance during charge/discharge cycling and thereby stabilizes the cells of Na-$NiCl_2$ batteries. Additionally, the simple film assembly offers a practical cell fabrication approach and is promising for large-scale production. However, the Na-$NiCl_2$ battery cycling performance must be further improved by addressing the issue of allowing higher liquid Na flux in the sparked rGO film for good rate capability, which is limited by the thickness and structure of the sparked rGO film. Although a simple methodology for fabricating batteries is unlikely to offer highly competitive cell performance, sparked rGO on the

DOI: 10.1021/acs.nanolett.9b03646
Nano Lett. 2019, 19, 8811−8820

β''-Al_2O_3 solid electrolyte is useful for the development of low-temperature NBBs.

■ ASSOCIATED CONTENT

Supporting Information

The Supporting Information is available free of charge at https://pubs.acs.org/doi/10.1021/acs.nanolett.9b03646.

Detailed experimental procedures, characterization, and images (PDF)

Movie S1: Spark reaction of the GO film (MP4)

Movie S2: Liquid Na infusion into the sparked rGO film (MP4)

■ AUTHOR INFORMATION

Corresponding Authors

*E-mail: joonlee@yonsei.ac.kr.

*E-mail: keeyoung.jung@rist.re.kr.

*E-mail: wshim@yonsei.ac.kr.

ORCID

Dana Jin: 0000-0001-9118-5693

Sangjin Choi: 0000-0002-1398-8391

Sungsoon Kim: 0000-0001-5124-7124

Keeyoung Jung: 0000-0002-3332-2335

Wooyoung Shim: 0000-0002-7601-6282

Author Contributions

○D.J. and H.G.L. contributed equally to this work.

Notes

The authors declare no competing financial interest.

■ ACKNOWLEDGMENTS

This work was supported by the National Research Foundation (NRF) of Korea through grants funded by the Korean government (2018M3D1A1058793, ERC-2015R1A5A1037668, and 2016M3A7B4910798). This work was also supported by grants from the International Collaborative Energy Technology R&D Program of the Korea Institute of Energy Technology Evaluation and Planning (KETEP) (20158510050010) and by the Institute for Basic Science (IBS-R026-D1).

■ REFERENCES

(1) Yang, Z.; Zhang, J.; Kintner-Meyer, M. C. W.; Lu, X.; Choi, D.; Lemmon, J. P.; Liu, J. *Chem. Rev.* **2011**, *111*, 3577−3613.

(2) Lu, X.; Xia, G.; Lemmon, J. P.; Yang, Z. *J. Power Sources* **2010**, *195*, 2431−2442.

(3) Hueso, K. B.; Armand, M.; Rojo, T. *Energy Environ. Sci.* **2013**, *6*, 734−749.

(4) Lu, X.; Li, G.; Kim, J. Y.; Lemmon, J. P.; Sprenkle, V. L.; Yang, Z. *Energy Environ. Sci.* **2013**, *6*, 1837−1843.

(5) Sudworth, J. L. *J. Power Sources* **2001**, *100*, 149−163.

(6) Sudworth, J. L.; Tilley, A. R. *The Sodium Sulfur Battery*; Chapman & Hall: London, 1985.

(7) Wen, Z.; Hu, Y.; Wu, X.; Han, J.; Gu, Z. *Adv. Funct. Mater.* **2013**, *23*, 1005−1018.

(8) Lu, X.; Li, G.; Kim, J. Y.; Lemmon, J. P.; Sprenkle, V. L.; Yang, Z. *J. Power Sources* **2012**, *215*, 288−295.

(9) Chang, H. J.; Lu, X.; Bonnett, J. F.; Canfield, N. L.; Son, S.; Park, Y. C.; Jung, K.; Sprenkle, V. L.; Li, G. *J. Power Sources* **2017**, *348*, 150−157.

(10) Hayashi, A.; Noi, K.; Sakuda, A.; Tatsumisago, M. *Nat. Commun.* **2012**, *3*, 856−860.

(11) Imai, A.; Harata, M. *Jpn. J. Appl. Phys.* **1972**, *11*, 180−185.

(12) Zhu, C.; Xue, J. *J. Alloys Compd.* **2012**, *517*, 182−185.

(13) Dunn, B.; Kamath, H.; Tarascon, J. M. *Science* **2011**, *334*, 928−935.

(14) Ragone, D. V. *Thermodynamics of Materials*; Wiley: New York, 1995; Vol. *II*, pp 97−126.

(15) Palmer, S. J. *Phys. Educ.* **1976**, *11* (2), 119−120.

(16) Viswanathan, L.; Virkar, A. V. *J. Mater. Sci.* **1982**, *17*, 753−759.

(17) Jin, D.; Choi, S.; Jang, W.; Soon, A.; Kim, J.; Moon, H.; Lee, W.; Lee, Y.; Son, S.; Park, Y. C.; Chang, H.; Li, G.; Jung, K.; Shim, W. *ACS Appl. Mater. Interfaces* **2019**, *11*, 2017−2924.

(18) de Gennes, P. G.; Brochard-Wyart, F.; Quéré, D. *Capillarity and Wetting Phenomena-Drops, Bubbles, Pearls, Waves*; Springer: New York, 2002; pp 1−31.

(19) Goldman, J. H. *J. Nucl. Mater.* **1984**, *126*, 86−88.

(20) Hu, Y.; Wen, Z.; Wu, X.; Lu, Y. *J. Power Sources* **2013**, *240*, 786−795.

(21) Reed, D.; Coffey, G.; Mast, E.; Canfield, N.; Mansurov, J.; Lu, X.; Sprenkle, V. *J. Power Sources* **2013**, *227*, 94−100.

(22) Ahlbrecht, K.; Bucharsky, C.; Holzapfel, M.; Tübke, J.; Hoffmann, M. J. *Ionics* **2017**, *23*, 1319−1327.

(23) Chang, H. J.; Lu, X.; Bonnett, J. F.; Canfield, N. L.; Han, K.; Engelhard, M. H.; Jung, K.; Sprenkle, V. L.; Li, G. *J. Mater. Chem. A* **2018**, *6*, 19703−19711.

(24) Factorovich, M. H.; Molinero, V.; Scherlis, D. A. *J. Am. Chem. Soc.* **2014**, *12* (136), 4508−4514.

(25) Lu, X.; Li, G.; Kim, J. Y.; Mei, D.; Lemmon, J. P.; Sprenkle, V. L.; Liu, J. *Nat. Commun.* **2014**, *5*, 4578−4585.

(26) Liu, Y.; Lin, D.; Jin, Y.; Liu, K.; Tao, X.; Zhang, Q.; Zhang, X.; Cui, Y. *Sci. Adv.* **2017**, *3*, No. eaao0713.

(27) Deng, W.; Zhou, X.; Fang, Q.; Liu, Z. *Adv. Energy Mater.* **2018**, *8*, 1703152.

(28) Wang, A.; Tang, S.; Kong, D.; Liu, S.; Chiou, K.; Zhi, L.; Huang, J.; Xia, Y. Y.; Luo, J. *Adv. Mater.* **2018**, *30*, 1703891.

(29) Wang, A.; Hu, X.; Tang, H.; Zhang, C.; Liu, S.; Yang, Y. W.; Yang, Q. H.; Luo, J. *Angew. Chem., Int. Ed.* **2017**, *56*, 11921−11926.

(30) Lin, D.; Liu, Y.; Liang, Z.; Lee, H. W.; Sun, J.; Wang, H.; Yan, K.; Xie, J.; Cui, Y. *Nat. Nanotechnol.* **2016**, *11*, 626−633.

(31) Pei, S.; Cheng, H. M. *Carbon* **2012**, *50*, 3210−3228.

(32) Sun, G.; Zheng, L.; Zhan, Z.; Zhou, J.; Liu, X.; Li, L. *Carbon* **2014**, *68*, 748−754.

(33) Gao, Y.; Chen, X.; Zhang, J.; Asakura, H.; Tanaka, T.; Teramura, K.; Ma, D.; Yan, N. *Adv. Mater.* **2015**, *27*, 4688−4694.

(34) Qiu, Y.; Moore, S.; Hurt, R.; Külaots, I. *Carbon* **2017**, *111*, 651−657.

(35) Qiu, Y.; Guo, F.; Hurt, R.; Külaots, I. *Carbon* **2014**, *72*, 215−223.

(36) Chen, Y.; Li, Y.; Wang, Y.; Fu, K.; Danner, V. A.; Dai, J.; Lacey, S. D.; Yao, Y.; Hu, L. *Nano Lett.* **2016**, *16*, 5553−5558.

(37) Krishnamoorthy, K.; Veerapandian, M.; Yun, K.; Kim, S. J. *Carbon* **2013**, *53*, 38−49.

(38) Huang, H. H.; De Silva, K. K. H.; Kumara, G. R. A.; Yoshimura, M. *Sci. Rep.* **2018**, *8*, 6849.

(39) Hussein, A.; Sarkar, S.; Kim, B. *J. Mater. Sci. Technol.* **2016**, *32*, 411−418.

(40) Chen, C. M.; Zhang, Q.; Yang, M. G.; Huang, C. H.; Yang, Y. G.; Wang, M. Z. *Carbon* **2012**, *50*, 3572−3584.

(41) Shulga, Y. M.; Baskakov, S. A.; Knerelman, E. I.; Davidova, G. I.; Badamshina, E. R.; Shulga, N. Y.; Skryleva, E. A.; Agapov, A. L.; Voylov, D. N.; Sokolov, A. P.; Martynenko, V. M. *RSC Adv.* **2014**, *4*, 587−592.

(42) Alothman, Z. A. *Materials* **2012**, *5*, 2874−2902.

(43) Guo, Z.; Li, J.; Xia, Y.; Chen, C.; Wang, F.; Tamirat, A. G.; Wang, Y.; Xia, Y.; Wang, L.; Feng, S. *J. Mater. Chem. A* **2018**, *6*, 6022−6032.

(44) Ossonon, B. D.; Bélanger, D. *RSC Adv.* **2017**, *7*, 27224−27234.

(45) Guo, F.; Creighton, M.; Chen, Y.; Hurt, R.; Külaots, I. *Carbon* **2014**, *66*, 476−484.

(46) Wu, N.; She, X.; Yang, D.; Wu, X.; Su, F.; Chen, Y. *J. Mater. Chem.* **2012**, *22*, 17254−17261.

DOI: 10.1021/acs.nanolett.9b03646
Nano Lett. 2019, 19, 8811−8820

(47) Dobrota, A. S.; Pašti, I. A.; Skorodumova, N. V. *Electrochim. Acta* **2015**, *176*, 1092−1099.
(48) Zhou, S.; Bongiorno, A. *Sci. Rep.* **2013**, *3*, 2484.
(49) Pei, A.; Zheng, G.; Shi, F.; Li, Y.; Cui, Y. *Nano Lett.* **2017**, *17*, 1132−1139.
(50) Wang, X.; Pan, Z.; Wu, Y.; Xu, G.; Zheng, X.; Qiu, Y.; Liu, M.; Zhang, Y.; Li, W. *Nanoscale* **2018**, *10*, 16562−16567.
(51) Wei, C.; Fei, H.; An, Y.; Tao, Y.; Feng, J.; Qian, Y. *J. Mater. Chem. A* **2019**, *7*, 18861−18870.

DOI: 10.1021/acs.nanolett.9b03646
Nano Lett. 2019, 19, 8811−8820